Available online at www.sciencedirect.com
SCIENCE DIRECT®
Journal of Sound and Vibration 282 (2005) 453–473
JOURNAL OF SOUND AND VIBRATION
www.elsevier.com/locate/jsvi

Theoretical and experimental study of efficient control of vibrations in a clamped square plate

Philip Shimon[a], Edmond Richer[b], Yildirim Hurmuzlu[a,*]

[a]*Department of Mechanical Engineering, Southern Methodist University, P.O. Box 750337, Dallas, TX 75275, USA*
[b]*Department of Radiological Sciences-9058, University of Texas Southwestern Medical Center, Dallas, TX 75235, USA*

Received 26 January 2002; accepted 28 February 2004
Available online 2 December 2004

Abstract

In this paper, we sought to develop an efficient controller for vibration reduction in a fully clamped plate. We investigated two control methodologies (positive velocity feedback and H_∞ control) and two types of actuators (an inertial actuator and a distributed strain actuator). These were used to develop four control architectures. Both theoretical and experimental studies were undertaken with varying results. The best theoretical results were obtained when H_∞ control was used in conjunction with a distributed strain actuator. Experimentally, the H_∞ controller using the distributed strain actuator outperformed the others.

1. Introduction

Active vibration control is not a new topic. Vibration isolation in vehicles and heavy equipment has been around since these machines were made. As technology changes and machines get more advanced, solutions become more complex. Smart structures have been employed for vibration control in applications ranging from skiis to spacecrafts. Piezoelectric material's properties make it an ideal choice in vibration suppression. The material can be integrated into a structural member and can be used as either a sensor or an actuator.

*Corresponding author.
E-mail address: hurmuzlu@engr.smu.edu (Y. Hurmuzlu).

0022-460X/$ - see front matter
doi:10.1016/j.jsv.2004.02.057

As aircraft continue to push limits, vibration fatigue of the air frame becomes a concern. Typically, passive control methods are susceptible to changes in the environmental conditions such as temperature variations. Therefore, active control methodologies can significantly improve vibration suppression in aircraft frames. Piezoelectric materials can be bonded to the aircraft frame and provide excellent vibration control with minimal spacial requirements. Coupled with control algorithms implemented on digital signal processors (DSPs), the entire system can be compact and meet space and weight restrictions.

Many proposed control solutions have used simple control algorithms to suppress the vibrations. Positive position [1], positive velocity [2], and state feedback control [3] have all been shown to yield acceptable outcomes. Also, there are a number of more complex controllers being used in vibration suppression. Adaptive position feedback [4] and neural networks [5], to name a few, have been used. But, there has been no rigorous comparison to simpler control methods to show that the performance benefits that arise from complexity is justifiable.

In this paper, we studied a fully clamped plate problem. Inertial actuators or distributed strain actuators were used. In addition, positive velocity feedback (PVF) and H_∞ control methods were used to suppress the first mode of vibration of the plate. Both theoretical and experimental studies were undertaken to identify the best suited actuator/control method for the problem at hand.

2. Plate modeling

For a fully clamped square plate, the governing equation for the lateral deflection with external excitation force f_{ex} and actuator force f_a is

$$D\left(\frac{\partial^2 w(x,y,t)}{\partial x^4}+2\frac{\partial^4 w(x,y,t)}{\partial x^2 y^2}+\frac{\partial^4 w(x,y,t)}{\partial y^4}\right)-\rho h\frac{\partial^2 w(x,y,t)}{\partial t^2} = f_{\text{ex}}(x,y,t)+f_a(x,y,t), \tag{1}$$

where $w(x,y,t)$ is plate transverse displacement; $D=Eh^3/(12(1-\nu^2))$, flexural rigidity; E, Young's modulus; ν, Poisson's ratio; ρ, density of the plate material; h, thickness of the plate; $f_{\text{ex}}(x,y,t)$, total force generated by the external excitation; and $f_a(x_a,y_a,t)$, total force generated by the actuator.

To analyze the normal modes of vibration we let $f_{\text{ex}}(x,y,t)=0$ and $f_a(x,y,t)=0$ and assume a solution of the form

$$w(x,y,t)=W(x,y)\mathrm{e}^{\mathrm{j}\omega t}. \tag{2}$$

Eq. (1) becomes

$$D\left(\frac{\partial^2 W(x,y)}{\partial x^4}+2\frac{\partial^4 W(x,y)}{\partial x^2 y^2}+\frac{\partial^4 W(x,y)}{\partial y^4}\right)-\rho h\omega^2 W(x,y)=0. \tag{3}$$

Assuming the edges are elastically restrained against rotation, the boundary conditions for Eq. (3) are given by (see Ref. [6])

$$\frac{\partial W}{\partial x}\left(\frac{\pm a}{2}, y\right) = \phi_x M_{1,x}\left(\frac{\pm a}{2}, y\right) = -\phi_x D\left[\frac{\partial^2 W}{\partial x^2} + \nu\frac{\partial^2 W}{\partial y^2}\right]_{x=\pm a/2}, \tag{4a}$$

$$\frac{\partial W}{\partial y}\left(x, \frac{\pm b}{2}\right) = \phi_y M_{1,y}\left(x, \frac{\pm b}{2}\right) = -\phi_y D\left[\frac{\partial^2 W}{\partial y^2} + \nu\frac{\partial^2 W}{\partial x^2}\right]_{y=\pm b/2}, \tag{4b}$$

where $M_x = M_{1,x}e^{j\omega t}$, $M_y = M_{1,y}e^{j\omega t}$ are the moments on the edges, and ϕ_x, ϕ_y are the rotation coefficients in the x and y directions, respectively. Using Galerkin's method, the displacement function is approximated by (see Ref. [11])

$$W(x, y) = \sum_{n=1}^{N} c_n W_n(x, y), \tag{5}$$

where $W_n(x, y)$ is the coordinate function for the nth mode, and c_n is the modal coefficient.

The coordinate functions for the first five modes are chosen as

$$W_1(x, y) = (\alpha_1 x^4 + \beta_1 x^2 + 1)(\alpha_1 y^4 + \beta_1 y^2 + 1), \tag{6a}$$

$$W_2(x, y) = x(\alpha_2 x^4 + \beta_2 x^2 + 1)(\alpha_2 y^4 + \beta_2 y^2 + 1), \tag{6b}$$

$$W_3(x, y) = y(\alpha_3 x^4 + \beta_3 x^2 + 1)(\alpha_3 y^4 + \beta_3 y^2 + 1), \tag{6c}$$

$$W_4(x, y) = xy(\alpha_4 x^4 + \beta_4 x^2 + 1)(\alpha_4 y^4 + \beta_4 y^2 + 1), \tag{6d}$$

$$W_5(x, y) = (x^2 - y^2)(\alpha_5 x^4 + \beta_5 x^2 + 1)(\alpha_5 y^4 + \beta_5 y^2 + 1). \tag{6e}$$

From the boundary conditions (4) one can determine the coefficients α_n and β_n for a square plate with elastically restrained edges as

$$\alpha_1 = \frac{16(a + 2D\phi)}{a^4(a + 10D\phi)}, \qquad \beta_1 = -\frac{8(a + 6D\phi)}{a^2(a + 10D\phi)}, \tag{7a}$$

$$\alpha_{2-4} = \frac{16(a + 6D\phi)}{a^4(a + 14D\phi)}, \qquad \beta_{2-4} = -\frac{8(a + 10D\phi)}{a^2(a + 14D\phi)}, \tag{7b}$$

$$\alpha_5 = \frac{16}{a^4}, \qquad \beta_5 = -\frac{8}{a^2}, \tag{7c}$$

where $\phi = \phi_x = \phi_y = 0.00355$ and $a = b$ for a square plate. These values were obtained experimentally in Ref. [7].

The modal coefficients c_n can be obtained normalizing the coordinate functions as follows:

$$\int_{-a/2}^{a/2}\int_{-a/2}^{a/2} \rho W_n(x,y) W_n(x,y)\,\mathrm{d}x\,\mathrm{d}y = 1, \quad n = 1,\ldots,5. \tag{8}$$

Substituting the coordinate functions (6) in the plate equation (3) and solving for ω we obtained the modal frequencies as

$$\omega_1 = \frac{\lambda_1\sqrt{D(a^4 + 36a^3D\phi + 472a^2D^2\phi^2 + \frac{23{,}192}{9}aD^3\phi^3 + \frac{41{,}640}{9}D^4\phi^4)}}{\alpha^2\sqrt{\rho h}(a^2 + 22aD\phi^2 + 124aD^2\phi^2)}, \tag{9a}$$

$$\omega_{12,21} = \frac{\lambda_{12,21}\sqrt{D(a^4 + 56a^3D\phi + \frac{132{,}352}{115}a^2D^2\phi^2 + \frac{1{,}169{,}472}{115}aD^3\phi^3 + \frac{3{,}688{,}200}{115}D^4\phi^4)}}{\alpha^2\sqrt{\rho h}\sqrt{(a^2 + 30aD\phi^2 + 228aD^2\phi^2) + (a^2 + 34aD\phi^2 + 300aD^2\phi^2)}}, \tag{9b}$$

$$\omega_4 = \frac{\lambda_4\sqrt{D(a^4 + \frac{4020}{67}a^3D\phi + \frac{90{,}360}{67}a^2D^2\phi^2 + \frac{891{,}000}{67}aD^3\phi^3 + \frac{3{,}223{,}800}{67}D^4\phi^4)}}{\alpha^2\sqrt{\rho h}(a^2 + 34aD\phi^2 + 300aD^2\phi^2)}, \tag{9c}$$

$$\omega_5 = \frac{\lambda_5\sqrt{D}}{\alpha^2\sqrt{\rho h}}, \tag{9d}$$

where λ_n are the modal frequencies coefficients.

The modal frequencies for the first five modes, computed with Eqs. (9) for a 0.032″ (0.8128 mm) (the one used in the experimental study) aluminum plate are presented in Table 1.

With the modal frequencies and shapes known, the forced vibration of the plate can be expressed as (see Ref. [8])

$$w(x,y,t) = \sum_{n=1}^{\infty} W(x,y)\eta_n(t), \tag{10}$$

where $\eta_n(t)$ are the time-dependent generalized coordinates. Substituting Eq. (10) into Eq. (1) and integrating over the entire domain of the plate we obtain the modal equations

$$\ddot{\eta}_n t + \omega_n^2 \eta_n t = N_m(t), \tag{11}$$

where $N_m(t)$ are the modal forces and ω_n are the modal frequencies (see next section).

Table 1
Eigenvalues and modal frequencies

mn	λ	f
11	36	257.25
12	74.296	547.66
21	74.296	547.66
22	108.59	813.89
33	137.294	1208.15

3. Actuator choices

Two different types of actuators were analyzed and tested. The first, an inertial actuator, used a piezoelectric material to vibrate a large mass. The vibration of this mass was used to counteract the vibration of the plate. The advantage of this type actuator was their capacity to apply large forces. Yet, this type of actuator was quite bulky and very heavy. In addition, because of the moving mass, it added two differential equations to the model. While this did not really pose a problem to the analysis, it added complexity. With the H_∞ controller, adding two equations to the plant increased the order of the controller by two, making it more complex and harder to implement. The equation of motion for the inertial actuator can be expressed as

$$M_a z'' + k_a[z_a(t) - w(x_a, y_a, t)] + c_a[z' - w(x_a, y_a, t)] = k_f V_a, \tag{12}$$

where M_a is the inertial mass, z_a is the inertial mass displacement in the vertical direction, x_a and y_a specify the actuator position on the plate, c_a is the internal damping coefficient, k_a is the internal spring constant, $w(x_a, y_a, t)$ is the plate displacement at the actuator position and k_f is the actuator gain and V_a is the applied voltage. The actuator force can be computed by solving for the inertia term ($M_a z''$). N_m (see Eq. (11)) can be computed using

$$N_m(t) = \int_D W_n(x, y) f_a(x_a, y_a, t). \tag{13}$$

Substituting Eq. (13) into Eq. (11), we get

$$\begin{aligned} \ddot{\eta}_n(t) + \omega_n^2 \eta_n(t) = W(x_a, y_a)[k_a[z_a(t) - w(x_a, y_a, t)] \\ + c_a[z' - w(x_a, y_a, t)] - k_f V_a]. \end{aligned} \tag{14}$$

The second type of actuator was a distributed strain actuator (patch). In this case, a layer of piezoelectric material was bonded to the plate. The actuator generated a strain on the plate to counteract the vibrations. This actuator had a very low mass and profile, could be manufactured to fit a specific shape, and added no additional complexity to the model. The disadvantage was that once bonded, it cannot be re-used if the plate was to be replaced. Assuming the patch does not significantly affect the dynamics of the plate, the equation of motion can be written as (see Ref. [9])

$$\begin{aligned} D\left(\frac{\partial^2 w(x, y, t)}{\partial x^4} + 2\,\frac{\partial^4 w(x, y, t)}{\partial x^2 y^2} + \frac{\partial^4 w(x, y, t)}{\partial y^4}\right) - \rho h\,\frac{\partial^2 w(x, y, t)}{\partial t^2} \\ = \frac{\partial^2 m_x}{\partial x^2} + \frac{\partial^2 m_y}{\partial y^2}, \end{aligned} \tag{15}$$

where

$$m_x = m_y = \tfrac{1}{12} K_1 E_p h_p^2\,\frac{d_{31}}{t_a}\,V_a, \tag{16}$$

where E_p is Young's modulus, h_p is the plate thickness and

$$K_1 = \frac{6\beta k(1+k)}{1+4\beta k+6\beta k^2+4\beta k^3+\beta^2 k^4}, \tag{17}$$

where we chose $\beta = E_{ep}/E_p$ and $k = t_a/h_p$ for simplicity.

The actuator forces can be computed using

$$N_m(t) = \int_D W_n(x,y)\left(\frac{\partial^2 m_x}{\partial x^2}+\frac{\partial^2 m_y}{\partial y^2}\right). \tag{18}$$

4. Control methods and simulation results

4.1. Positive velocity feedback

PVF is the most basic control approach. The velocity of the plate is amplified with a gain K and fed back into the actuator; see Fig. 1. For the inertial actuator, a gain (k_f) of 50,000 was used in the simulations (see Eq. (14)). We arrived at this gain by increasing the gain until we reached a physical limit, set by the voltage level that can be applied to the actuator. Similarly, for the patch, a gain of 500,000 was used. Figs. 2 and 3 show the simulation results for the inertial and the patch actuators, respectively. As can be seen from the figures, the patch actuator produces better results. We attribute this difference to the fact that the patch acts over an area while the inertial actuator applies a point force.

4.2. H_∞ control

The method of H_∞ control was chosen for this system because of its robust properties [12,13]. The design methodology is straightforward and adopted from Ref. [10]. The controller is based on the state-space parameters of the plant and a parameter, γ. In the optimization of the controller, γ is reduced until a certain set of design specifications are met or the controller fails to converge. To facilitate the design process, weights can be introduced into the system. These weights are not used in the real system but rather used to tune the frequency response of the controller (see Fig. 4). In this figure, there are two inputs, a disturbance D and a noise input N. In addition, Z_1 and Z_2 are the outputs of the plant and controller, respectively. The realization, K, represents the H_∞

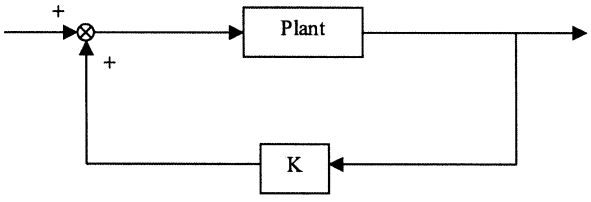

Fig. 1. Block diagram of the PVF controller design.

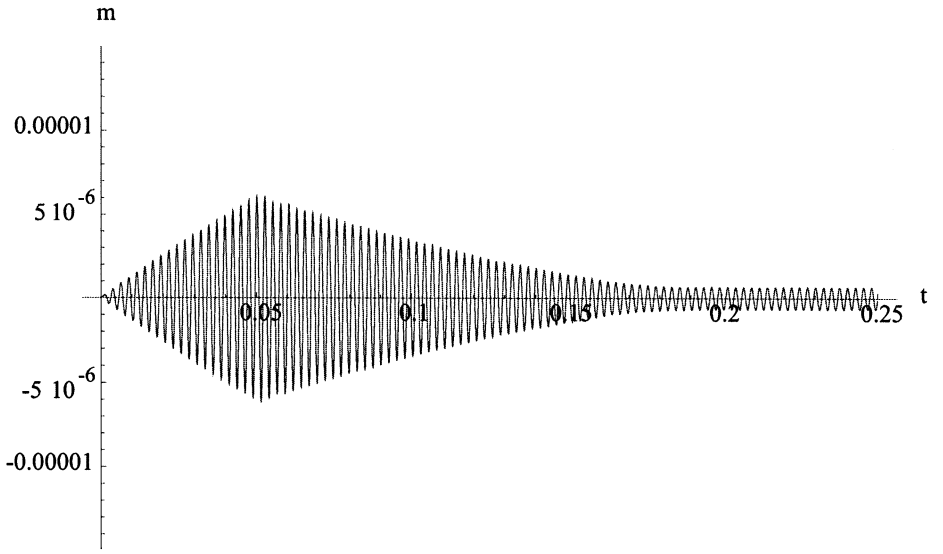

Fig. 2. PVF using an inertial actuator.

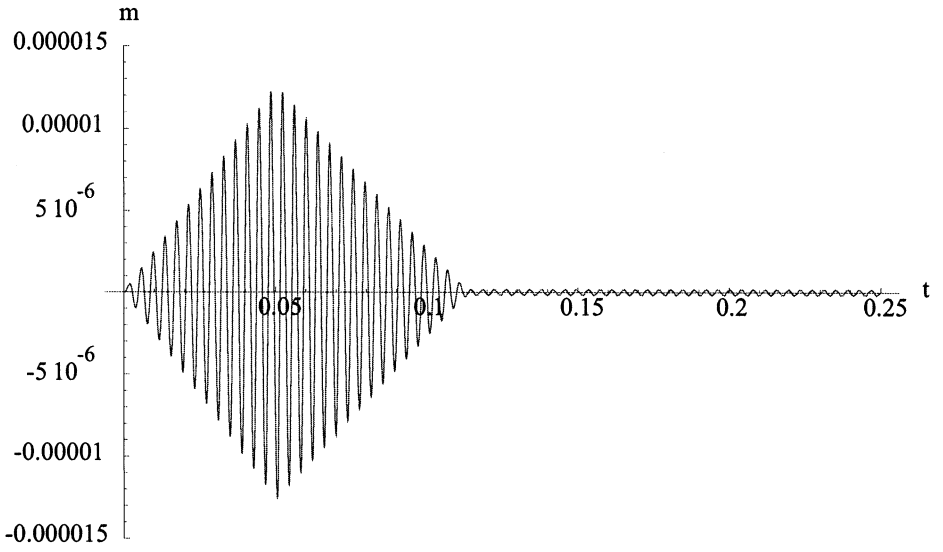

Fig. 3. PVF using a distributed strain actuator.

control. The system matrices A_P, B_{1P}, B_{2P}, and C_P area the state-space representation of the plant (see Eqs. (11) and (18)). In both the inertial actuator and the patch systems, two constant weights (W_1 and W_2) and two weights that are polynomials in the frequency domain (W_3 and W_4) are implemented. These weights are applied to the inputs and outputs as shown in Fig. 4. The weights will be chosen and optimized to achieve the desired performance. The order of the H_∞ controller is equal to the order of the plant plus the orders of the frequency dependent weights. A trade off

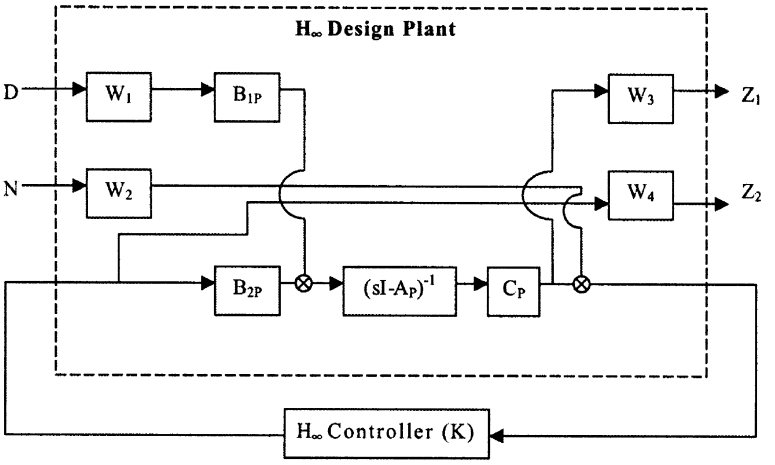

Fig. 4. Block diagram of the H_∞ controller design.

between using complex weights to achieve the desired performance and having a very high-order controller is necessary in choosing the order of the weight functions.

The H_∞ approach attempts to minimize the H_∞ norm, $\|T\|_\infty$, where the norm is defined as

$$\|T\|_\infty = \sup \sigma_{\max}[(T_{zw})_{ij}] \quad \forall i,\ j<\gamma, \tag{19}$$

where $(T_{zw})_{ij}$ are the transfer functions of a multi-input, multi-output system:

$$\begin{bmatrix} Z_1 \\ Z_2 \end{bmatrix} = \begin{bmatrix} (T_{zw})_{11} & (T_{zw})_{12} \\ (T_{zw})_{21} & (T_{zw})_{22} \end{bmatrix} \begin{bmatrix} D \\ N \end{bmatrix}. \tag{20}$$

In addition, γ is a parameter that should be minimized.

For the present system, there are four possible functions to minimize

$$T_{zw}(s) = \begin{bmatrix} W_1 W_3 G_1 S & W_2 W_3 C_P \\ W_1 W_4 G_1 K S & W_2 W_4 K S \end{bmatrix}, \tag{21}$$

where $G_1 = C_P(sI - A_P)^{-1}B_{1P},\ G_2 = C_P(sI - A_P)^{-1}B_{2P},\ S = (I - G_2K)^{-1}$.

One can see from the system matrix (21) that by manipulating the weights, the frequency response can change. The solution of Eq. (21) can be obtained by selecting a feedback function K of the following form (see Ref. [10] for details):

$$K = \begin{bmatrix} A - B_2K_c - Z_\infty K_\varepsilon C_2 + \gamma^{-2}(B_1B_1' - Z_\infty K_\varepsilon D_{21}B_1')X_\infty & Z_\infty K_\varepsilon \\ -K_c & 0 \end{bmatrix}, \tag{22}$$

where $K_c = \tilde{D}_{12}(B_2'X_\infty + D_{12}'C_1),\ K_\varepsilon = (Y_\infty C_2' + B_1D_{21}')\tilde{D}_{21},\ Z_\infty = (I - \gamma^{-2}Y_\infty X_\infty)^{-1}$.

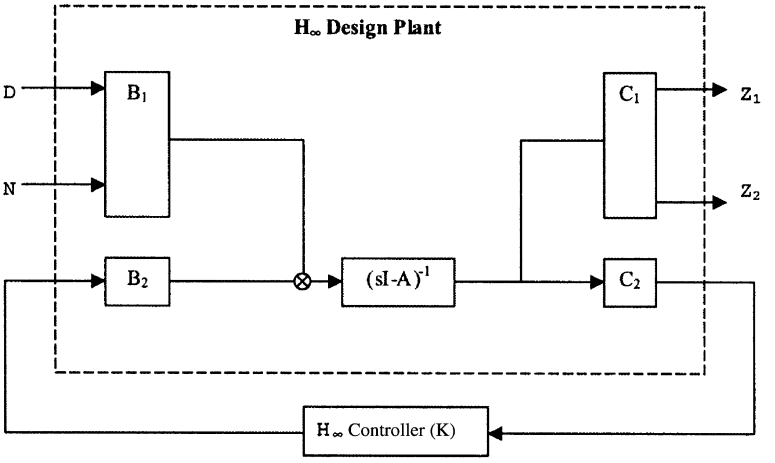

Fig. 5. Block diagram of the H_∞ controller design.

In addition, the functions X_∞ and Y_∞ can be obtained from the solution of the following Ricatti equations (see Ref. [10]):

$$X_\infty = \mathrm{Ric}\begin{bmatrix} A - B_2\tilde{D}_{12}D_{12}'C_1 & \gamma^{-2}B_1B_1' - B_2\tilde{D}_{12}B_2' \\ -\tilde{C}_1'\tilde{C}_1 & -(A - B_2\tilde{D}_{12}D_{12}'C_1)' \end{bmatrix}, \tag{23}$$

$$Y_\infty = \mathrm{Ric}\begin{bmatrix} (A - B_1D_{21}'\tilde{D}_{21}C_2)' & \gamma^{-2}C_1'C_1 - C_2'\tilde{D}_{21}C_2 \\ -\tilde{B}_1\tilde{B}_1' & -(A - B_1D_{21}'\tilde{D}_{21}C_2) \end{bmatrix}, \tag{24}$$

where $\tilde{D}_{12} = (D_{12}'D_{12})^{-1}$, $\tilde{D}_{21} = (D_{21}D_{21}')^{-1}$, $\tilde{C}_1 = (I - D_{12}\tilde{D}_{12}D_{12}')C_1$, $\tilde{B}_1 = B_1(I - D_{21}'\tilde{D}_{21}D_{21})$.

In the above equations, the matrices A, B_1, B_2, C_1, C_2, D_{11}, D_{21}, D_{12}, and D_{22} are the state-space representation of the system with the states of the plant and the weights combined (see Fig. 5):

$$A = \begin{bmatrix} A_P & 0 & 0 \\ B_{W3}C_P & A_{W3} & 0 \\ 0 & 0 & A_{W4} \end{bmatrix}, \quad B_1 = \begin{bmatrix} W_1B_{1P} \\ 0 \\ 0 \end{bmatrix}, \quad B_2 = \begin{bmatrix} B_{2P} \\ 0 \\ B_{W4} \end{bmatrix}, \tag{25}$$

$$C_1 = \begin{bmatrix} D_{W3}C_P & C_{W3} & 0 \\ 0 & 0 & C_{W4} \end{bmatrix}, \quad D_{11} = [0], \quad D_{12} = \begin{bmatrix} 0 \\ D_{W4} \end{bmatrix}, \tag{26}$$

$$C_2 = [C_{2P}\ 0\ 0], \quad D_{21} = [0\ W_2], \ D_{22} = [0]. \tag{27}$$

Finally, the controller will be stable if $\lambda_{\max}(X_\infty Y_\infty) < \gamma^2$, where $\lambda_{\max}$ is the largest eigenvalue of $X_\infty Y_\infty$. If this condition is met, then γ can be reduced and the Ricatti equations solved again. This continues until the largest eigenvalue of $X_\infty Y_\infty$ is less than γ^2, where the previous iteration becomes the controller.

4.2.1. Inertial actuator

The control for the inertial actuator is the more complex of the two control systems because the modeling of the actuator itself adds a second-order differential equation. We are only interested in the first mode of vibration because we are placing the inertial actuator in the center of the plate. The placement of the actuator allows it to excite—and therefore control—only the first mode. The dynamics of the inertial actuator is modeled with a second-order differential equation. Thus, the system can be modeled by two second-order differential equations:

$$\eta_1'' + \omega^2\eta_1 = c(k_a(z - c\eta_1) + c_a(z' - c\eta_1') - kfV) + cF_{\text{ex}}, \tag{28}$$

$$M_a z'' + k_a(z - c\eta_1) + c_a(z' - c\eta_1) = k_f V, \tag{29}$$

where F_{ex} is the excitation force; ω the modal frequency, 1616.33; c the modal coefficient, 0.2849; k_a the actuator gain, 314911; c_a the actuator damping, 25.6767; k_f the voltage of force conversion, 0.067; M_a the actuator mass, 0.118; and V the controller voltage.

In these equations η is the generalized coordinate, z is the displacement of the inertial mass of the actuator from the rest position of the plate. For the inertial actuator system, the weights used in the design were

$$W_1 = 500, \quad W_2 = 5 \times 10^{-5}, \quad W_3 = \frac{15{,}000}{6.19579 \times 10^{-5} + 1},$$
$$W_4 = 0.125\,\frac{1.04167 \times 10^{-7}s + 1}{2.5 \times 10^{-8}s + 1}. \tag{30–33}$$

The controller found under these conditions was a sixth-order system given by

$$A_C = \begin{bmatrix} 0 & 1 & 0 & 0 & 0 & 0 \\ -3.16 \times 10^6 & -4.06 \times 10^6 & 1.11 \times 10^5 & 2.89 \times 10^1 & -1.79 \times 10^6 & 2.51 \times 10^8 \\ 0 & 2.85 \times 10^{-1} & 0 & 1 & 0 & 0 \\ 1.63 \times 10^7 & -8.55 \times 10^3 & -3.29 \times 10^6 & -8.59 \times 10^2 & 5.26 \times 10^7 & -7.45 \times 10^9 \\ 2.74 \times 10^7 & -1.51 \times 10^4 & -1.09 \times 10^6 & -1.13 \times 10^3 & -7.38 \times 10^6 & -1.32 \times 10^{10} \\ 0 & 0 & 0 & 0 & 1 & 0 \end{bmatrix}, \tag{34}$$

$$B_C = \begin{bmatrix} 3.93 \times 10^{-8} \\ 3.28 \times 10^7 \\ -2.30 \\ 5.02 \times 10^2 \\ 0 \\ 0 \end{bmatrix}, \tag{35}$$

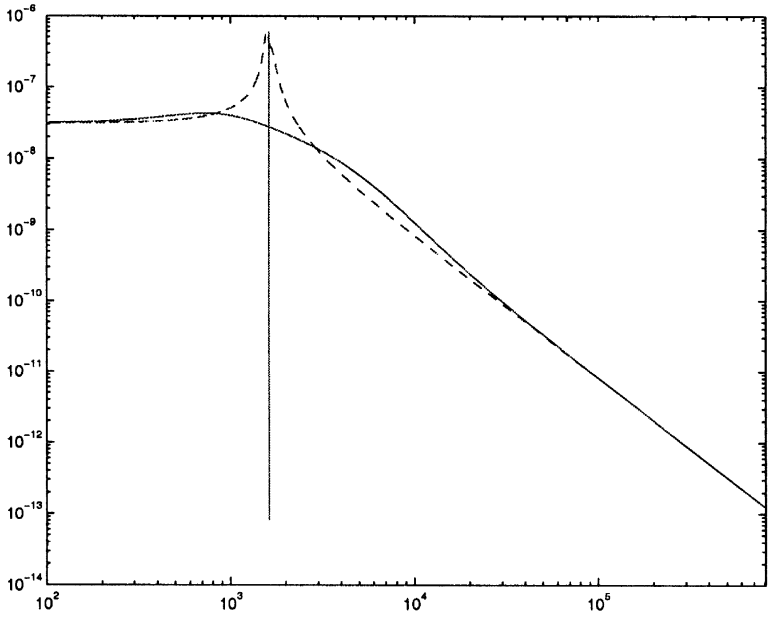

Fig. 6. Frequency response of the inertial actuator system, with the dashed curve for the original system; solid curve for the closed-loop system.

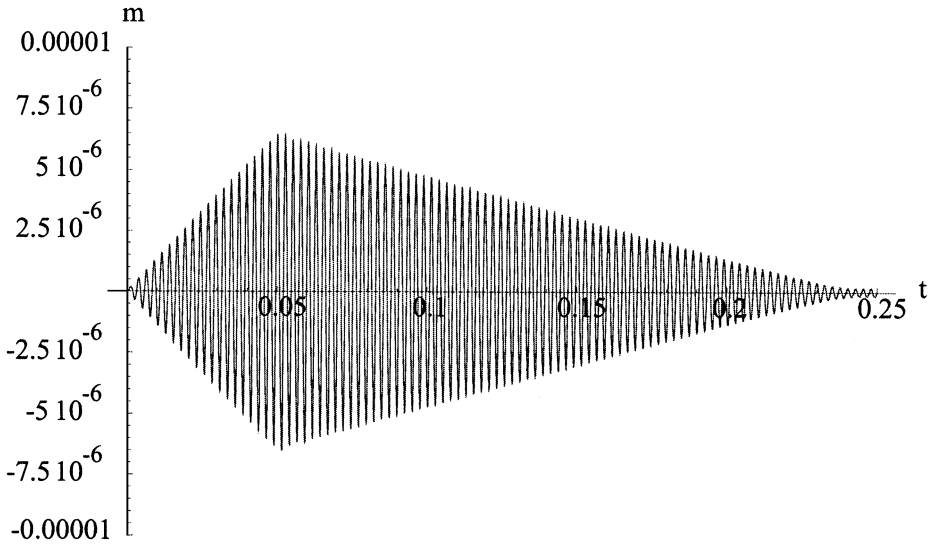

Fig. 7. Simulated results of the inertial actuator control.

$$C_C = [1.19 \times 10^1 \ -6.53 \times 10^{-3} \ -4.72 \times 10^{-1} \ -4.90 \times 10^{-4} \ 4.02 \times 10^1 \ -5.69 \times 10^3], \quad (36)$$

$$D_C = [0]. \quad (37)$$

The frequency response of the system with and without the controller is shown in Fig. 6.

The closed-loop system, including an external disturbance acting at the resonant frequency of the first mode of the plate, was implemented in a symbolic module in Mathematica 3.0 and tested numerically. The vibration in the plate started to build up until the controller was turned on. At that time, the controller hit the maximum voltage allowed to the inertial actuator (80 V). The actuator saturated but continued to damp out the vibrations. The residual vibration of the plate eventually reached a steady-state magnitude of 1.5×10^{-8} m. Fig. 7 shows the simulated results.

4.2.2. Distributed strain actuator

The H_∞ approach taken above was then utilized for the distributed strain actuator. The distributed strain actuator offers the advantages of low weight and simpler modeling. In this case, the distributed strain actuator is attached to the plate and has negligible mass. Therefore, the equation of motion of the plate is not altered. This allows us to model the system with one second-order differential equation:

$$\eta_1'' + \omega^2 \eta_1 = N_m V + cF_{\text{ex}}, \tag{38}$$

where F_{ex} is the excitation force; ω the modal frequency, 1616.33; c the modal coefficient, 0.2849; N_m the modal force, 0.02004 (see Eq. (18)); and V the controller voltage.

Again, η represents the generalized coordinate of the system.

During implementation, one should monitor the spill-over effects into higher modes. However, the symmetry of the distributed strain actuator about the center of the plate ensures that spill-over

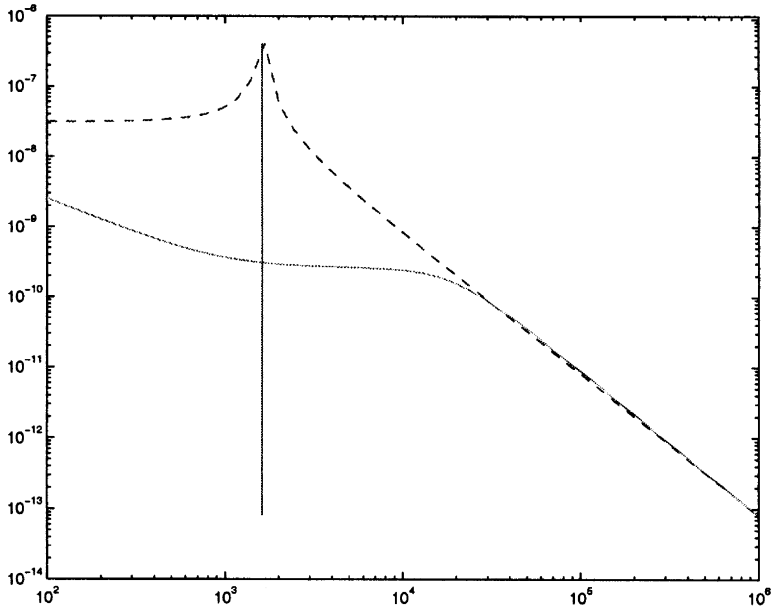

Fig. 8. Frequency response of the H_∞ controller with the patch, with the dashed curve for the original system; solid curve for the closed-loop system.

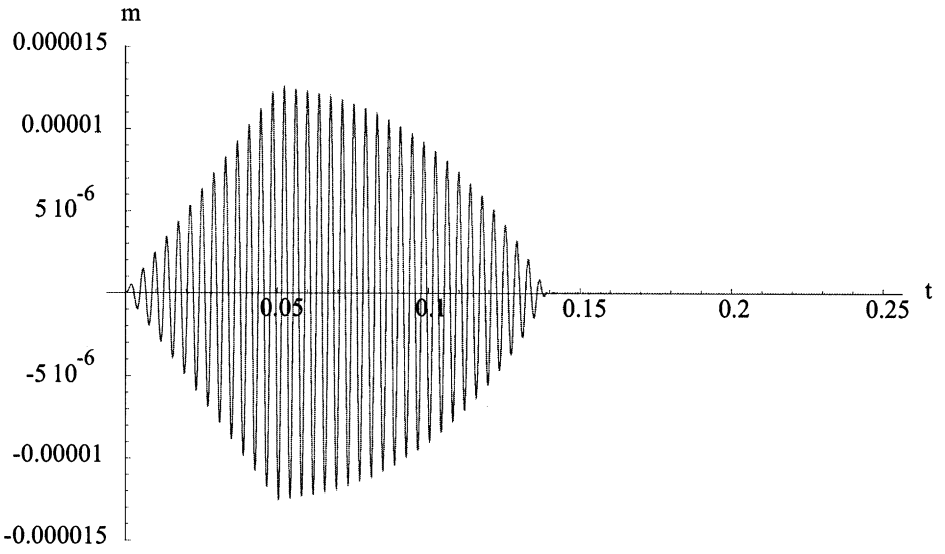

Fig. 9. Time-domain response of the H_∞ controller with the distributed strain actuator.

effects are absent. The weights chosen for this design are given as

$$W_1 = 5, \quad W_2 = 1.8 \times 10^{-6}, \quad W_3 = \frac{1 \times 10^6}{\frac{s}{1614} + 1}, \quad W_4 = \frac{\frac{1}{160}(\frac{s}{6000} + 1)}{\frac{s}{4000} + 1}. \tag{39–42}$$

With a second-order plant and two first-order weights, a fourth-order controller was designed. The frequency response of the system is shown in Fig. 8.

The state-space matrices of the resulting controller were given by

$$A = \begin{bmatrix} 0 & 1.704 & 6390 & 0 \\ -2.192 \times 10^6 & -2.303 \times 10^5 & -1.824 \times 10^8 & 6.657 \times 10^5 \\ 0 & 4.608 \times 10^{-3} & -929.8 & 0 \\ 2.101 \times 10^7 & -2.390 \times 10^5 & -9.402 \times 10^9 & -6.784 \times 10^6 \end{bmatrix}, \tag{43}$$

$$B = \begin{bmatrix} -84{,}517 \\ 2.7064 \times 10^10 \\ 33{,}644 \\ 0 \end{bmatrix}, \tag{44}$$

$$C = [614.32 \quad -6.9902 \quad -2.7494 \times 10^5 \quad 971.3], \quad D = [0]. \tag{45,46}$$

This controller was simulated under the same test conditions as the first case. The results showed that the distributed strain actuator was able to achieve better control than the inertial actuator. Fig. 9 shows the time domain results of the controller.

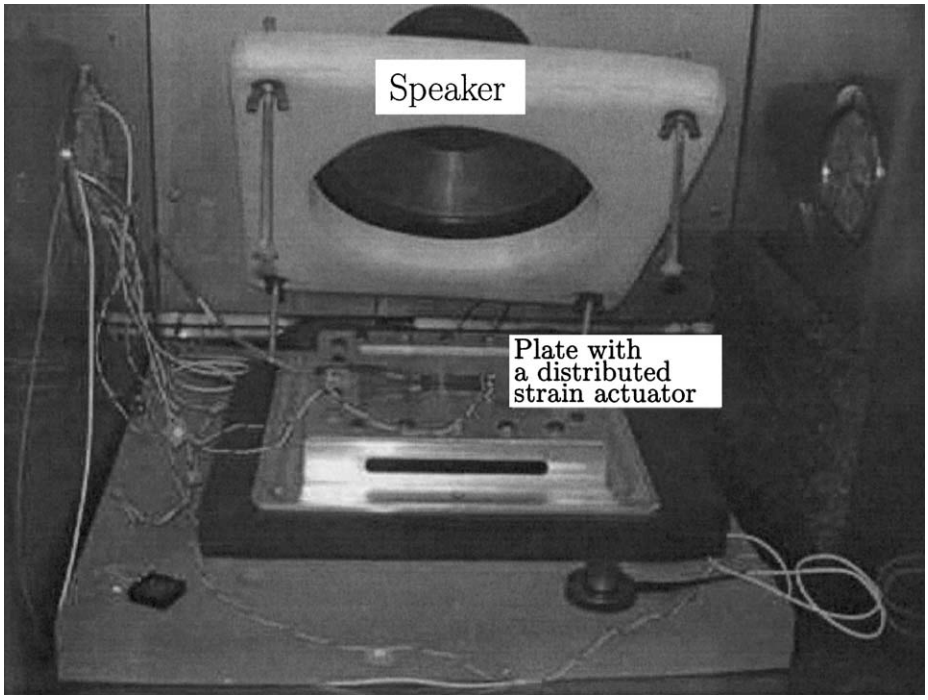

Fig. 10. Experimental test setup: plate and speaker.

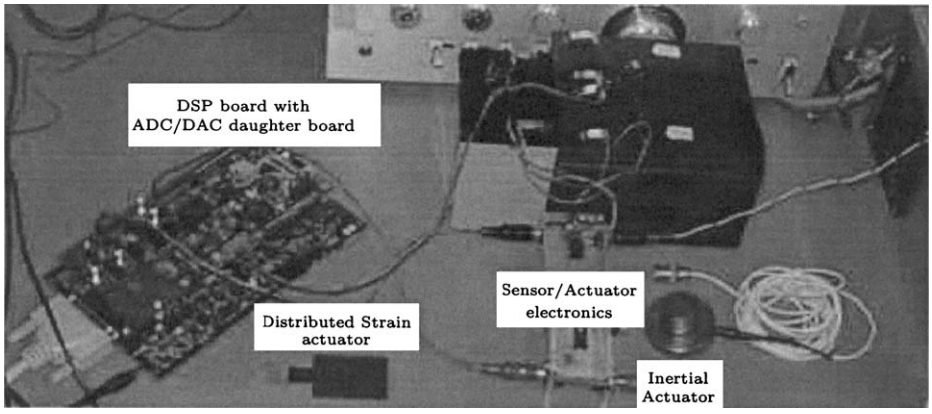

Fig. 11. Experimental test setup: electronics.

5. Experimental results

To verify the analysis, an experimental test setup was created. A $6'' \times 6''$ (15.24 cm $\times$ 15.24 cm) aluminum plate with a thickness of $0.032''$ (0.8128 mm) is mounted in an aluminum frame. A

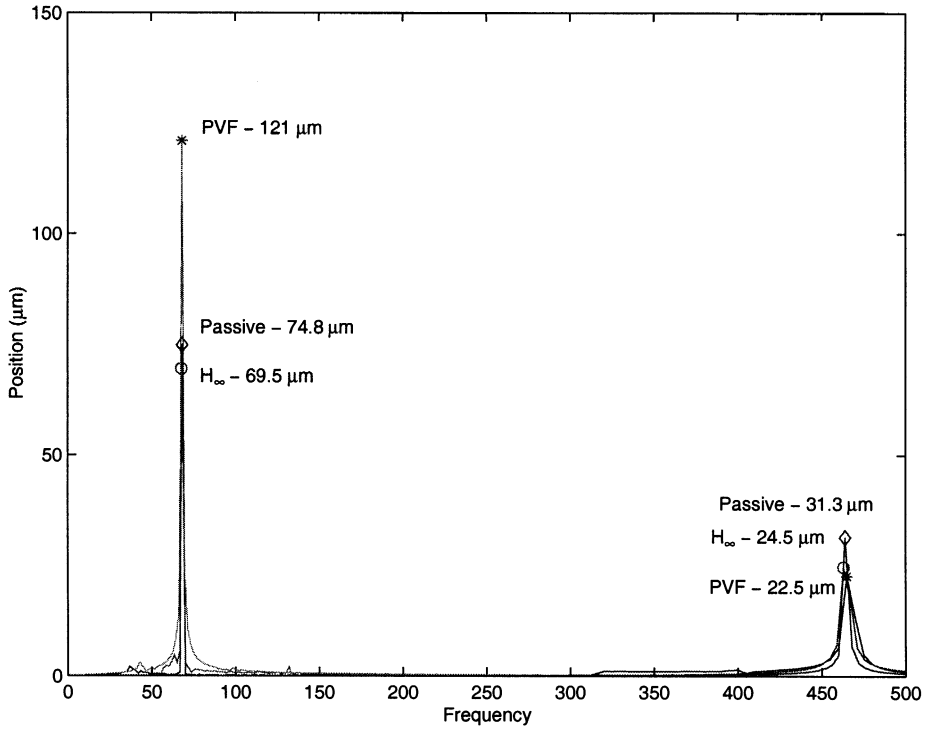

Fig. 12. Frequency response of controllers using the inertial actuator, with solid curve and diamond markers for no control (first max. of 74.8 mm and second max. of 31.3 mm); dotted curve and star markers for PVF (first max. of 121 μm and second max. of 22.5 μm); and dashed curve and circular markers for H_∞ (first max. of 69.5 μm and second max. of 24.5 μm).

speaker is placed over the plate to generate the external excitations (see Fig. 10). Because the initial impetus for this design was to use the controller on an aircraft, the electronics were chosen with that environment in mind. The control algorithms are implemented on a 150 MHz TI 6711 Floating Point digital signal processor (DSP) with a TLV2541 analog-to-digital converter (ADC) and a TLV5636 digital-to-analog converter (DAC). Analog circuitry is used to power the accelerometers and condition the signal before the ADC and an amplifier is used to amplify the signal from the DSP to the actuators (see Fig. 11).

5.1. Inertial actuator

Two controllers were implemented with the inertial actuator, PVF and H_∞. Because of noise in the system, the controller's gain had to be reduced from the theoretical values to achieve stability. The gains were reduced by three orders of magnitude for both the PVF and H_∞. When the inertial actuator was added, the combined effect of the second degree of freedom and the inherent passive damping was observed as two new natural frequencies with lower amplitude vibrations. The two new natural frequencies are at 70 and 465 Hz (the natural frequency of the bare plate was

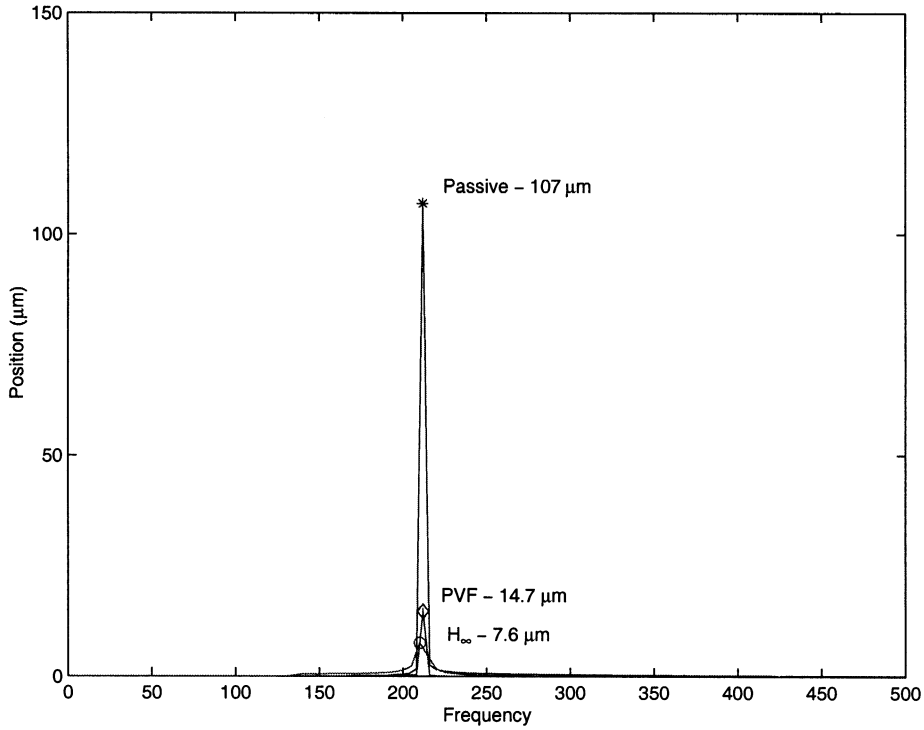

Fig. 13. Frequency response of controllers using the patch, with solid curve and star markers for no control (max. of 107 μm); dotted curve and diamond markers for PVF (max. of 14.7 μm); and dashed curve and circular markers for H_∞ (max. of 7.6 μm).

at 212 Hz). In addition, the lowered magnitudes at the two natural frequencies were 74.8 and 31.3 μm a reduction of 30% and 71%, respectively (the resonant magnitude of the bare plate was 107 μm).

The PVF controller further reduced the vibrations at 465 Hz 28% from the actuator off level for a total reduction of 79%. However, at 70 Hz, the vibrations increased 62% for a total increase of 13%. The H_∞ controller was able to reduce the vibrations at both frequencies (7% at 70 Hz and 22% at 465 Hz) for a total reduction of 35% and 77% at 70 and 465 Hz, respectively. The results are shown in Fig. 12.

5.2. Distributed strain actuator

The same two control methodologies used with the inertial actuator were used with the patch. Again, the gain had to be reduced from theoretical values to stabilize the system. In this case, the gain was reduced by three and four orders of magnitude for the PVF and H_∞, respectively. Using the speaker to excite the plate at 212 Hz, the PVF was able to reduce the vibrations by 86%. The H_∞ controller showed the best performance with a 93% reduction in the vibrations. Fig. 13 shows the results of the controllers.

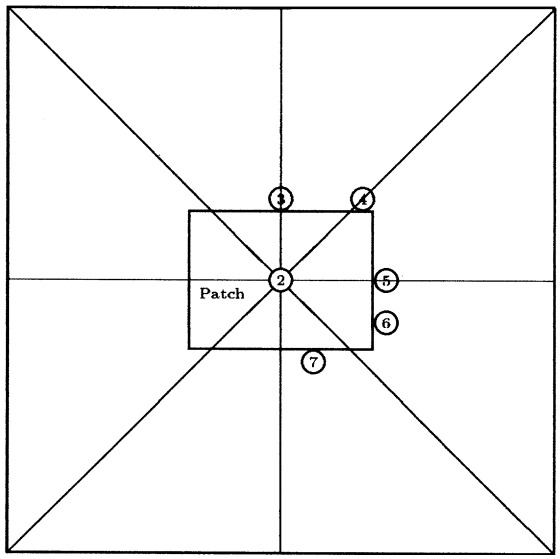

Fig. 14. Accelerometer placement on plate. Position 1 is on the backside, in the center.

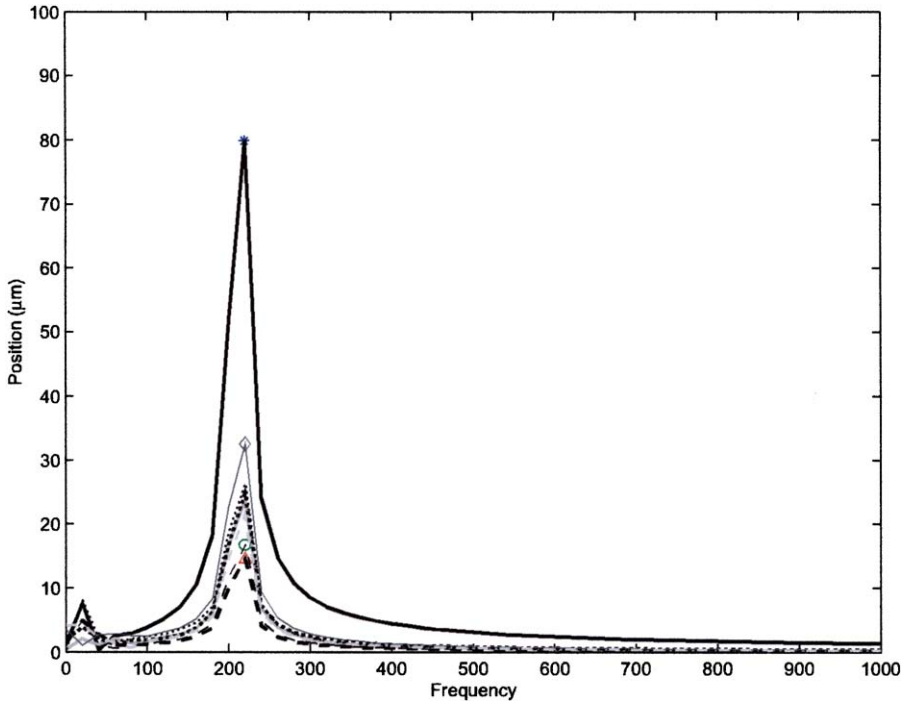

Fig. 15. Accelerometer placement test using PVF. Excitation at 212 Hz, with thick solid curve and star markers for no control; thick dashed curve and circular markers for position 1 (backside); thin dashed curve and triangular markers for position 2; solid gray curve for position 3; thin dotted curve for position 4; thick dotted curve for position 5; thin solid curve and diamond markers for position 6; and dashed gray curve for position 7.

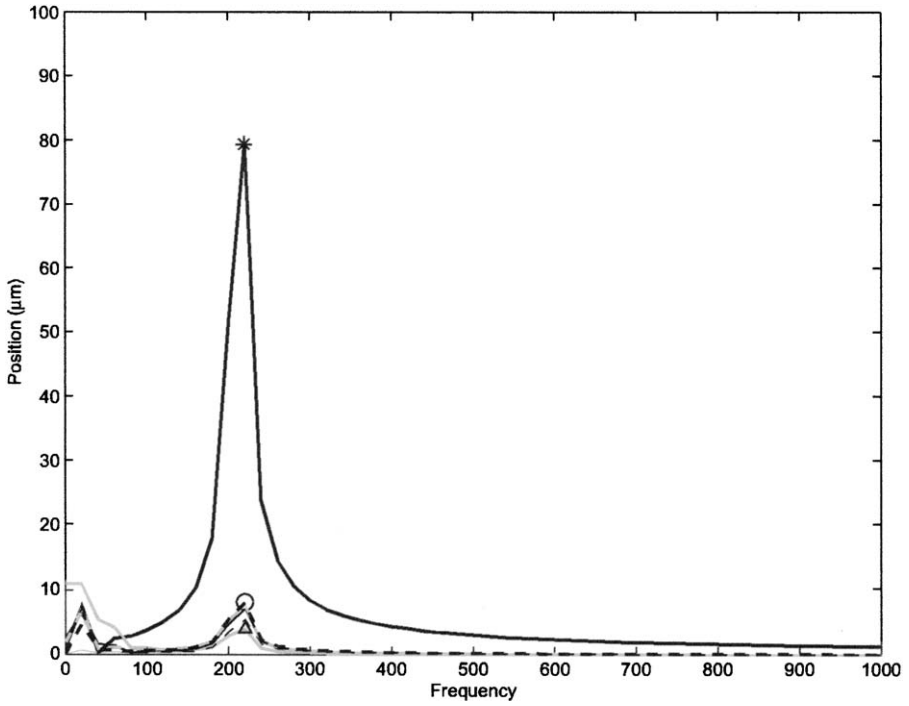

Fig. 16. Accelerometer placement test using H_∞. Excitation at 212 Hz, with thick black curve and star markers for no control (max. at 79.9 μm); thick dashed black curve and circular markers for position 1 backside (max. at 8.17 μm, 90% reduction); thin gray curve for position 2 (max. at 4.1 μm, 95% reduction); thick gray curve and triangular markers for position 3; thick dashed gray curve for position 4; thin dashed black curve for position 5; thin black curve for position 6; and thin dashed gray curve for position 7.

5.3. *Accelerometer placement*

The above results were obtained when the accelerometer was placed on the opposite side from the patch, in the very center of the plate. Because this would represent the outside of the aircraft, several tests were conducted to see how the controllers responded to varying placement of the accelerometer on the same side as the patch. Fig. 14 depicts the different locations used when the accelerometer was placed at six distinct locations on the same side of the patch. Note that the original placement on the backside of the plate was labelled as location one. In all these cases, the accelerometer number one was used to collect the measurement data (not for feedback).

The tests were conducted with an excitation frequency of 212 and 500 Hz (the 1st and 2nd modal frequencies, found experimentally). The vibration reduction when using PVF control with an excitation frequency of 212 Hz, strongly depends on accelerometer placement (Fig. 15). Positions 1 and 2 showing the best attenuation (79% and 80% reduction, respectively) while position 6 results in the lowest attenuation (59% reduction). For the H_∞ controller, the results showed minor dependence on accelerometer placement with vibration reductions ranging from 90% to 95% for position one and position two, respectively (see Fig. 16).

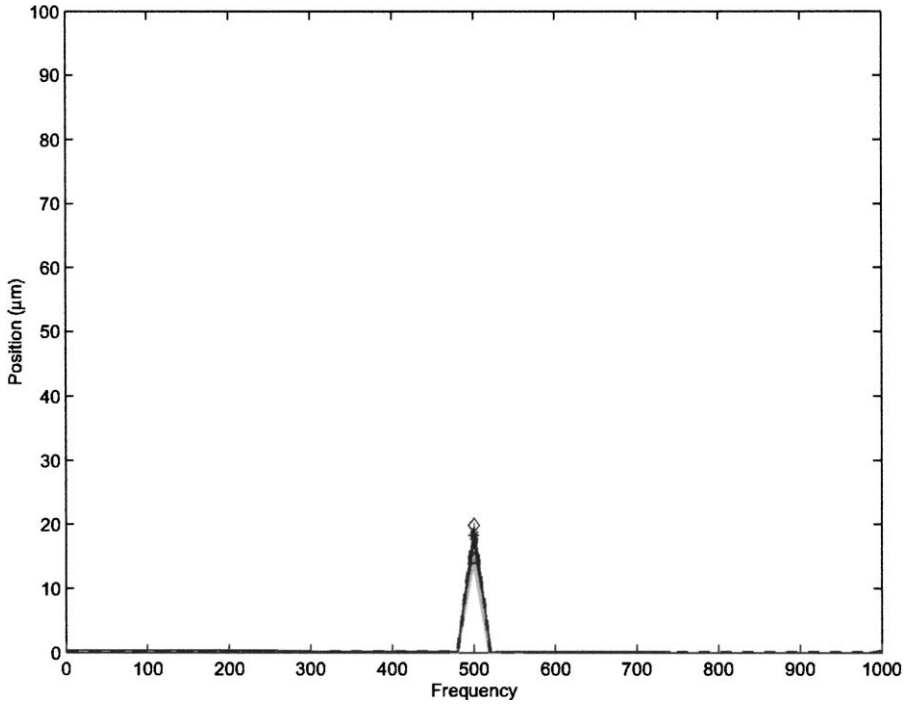

Fig. 17. Accelerometer placement test using PVF. Excitation at 500 Hz, with thick black curve and star markers for no control; thin black curve and circular markers for position 1 backside (max. at 14.8 μm, 19% reduction); thick gray curve and triangular markers for position 2 (max. at 14.5 μm, 21% reduction); thick dashed black curve and diamond markers for position 3 (max. at 19.9 μm, 9% increase); thin dashed black curve for position 4; dashed black curve for position 5; black curve for position 6; and gray curve for position 7.

When the plate was excited at 500 Hz, neither controller resulted in significant vibration attenuation (there was even minor amplification in a few cases). When there was amplification, it was very small (9% for the PVF and 9% for the H_∞ controller). This shows that while there was some spill-over into the second and third modes of vibration, the spill-over was negligible. Figs. 17 and 18 show the results of the 500 Hz excitation experiments.

It can be seen that the choice of accelerometer placement is dependent on the control algorithm. In both cases, position 1 shows good results but is not feasible in the actual design since the accelerometer would be mounted outside the aircraft. Position 2 or 5 could be chosen for the H_∞ controller and position 7 for the PVF controller.

6. Conclusions

In this paper, four control architectures were developed and tested to control the first mode of a 6″ (15.24 cm) square aluminum plate that was acoustically excited. The algorithms used two different actuators and two different control methodologies. Accelerometer placement was tested using two of the controllers to determine how location affected performance.

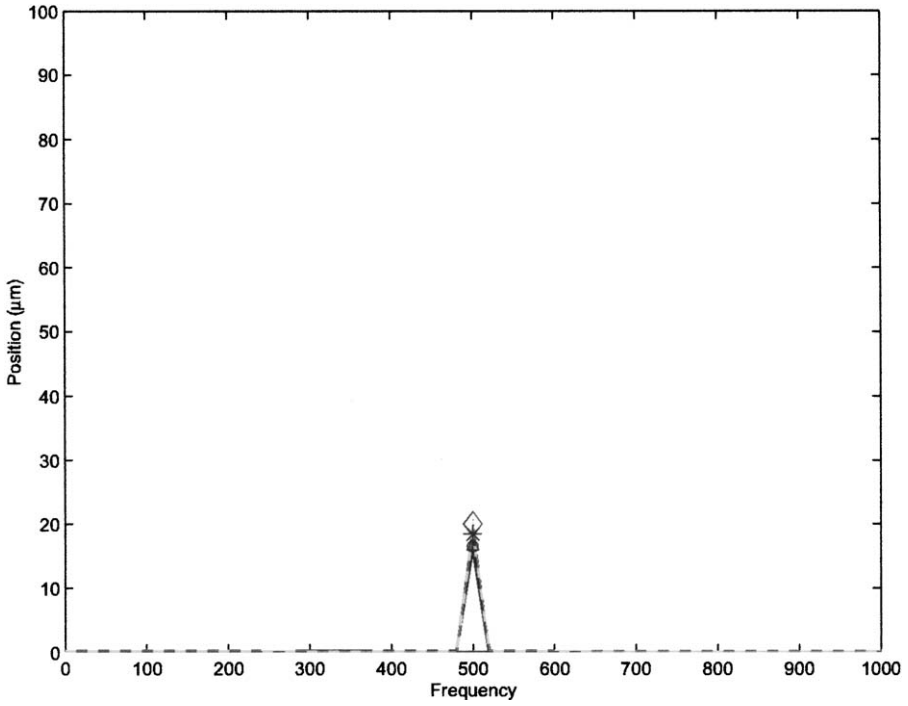

Fig. 18. Accelerometer placement test using H_∞, Excitation at 500 Hz, with thick dashed gray curve and star markers for no control; thin gray curve and circular markers for position 1 backside (max. at 16.4 μm, 10% reduction); thick black curve and triangular markers for position 2 (max. at 16.4 μm, 10% reduction); thin black curve and diamond markers for position 3 (max. at 19.9 μm, 9% increase); thin dashed black curve for position 4; dashed black curve for position 5; black curve for position 6; and gray curve for position 7.

Positive velocity control and H_∞ control were implemented with the inertial actuator. These controllers exhibited good performance in simulation but did not perform as well in the experiments. The inertial actuator adds a second degree of freedom to the system dynamics because of the resonating mass. This produces two resonant frequencies. In simulations, these two frequencies were very close to each other. However, the added weight of the inertial actuator on the plate was not modeled so the natural frequency of the plate in simulation was higher than in the experiments. Both the PVF and H_∞ controllers performed well at the higher frequency (77% and 79%, respectively). Yet the performance of the H_∞ controller was superior to the PVF controller at the lower frequency (35% attenuation vs. 7% amplification).

The distributed strain actuator was also used with PVF and H_∞ controllers. The simulation results in this case were outstanding. The experimental results, perhaps not as much as the simulation, were also excellent. The H_∞ controller outperformed the PVF (93% reduction in vibrations vs. 80% for PVF).

The experimental results, while good, did not perform as well as the theoretical results, mainly due to saturation of the accelerometer and delay in the system. Saturation due to high-frequency noise and the digitizing effects of the DAC were not accurately modeled. In order to prevent saturation in the experiments, the gain of the controllers had to be reduced. A small displacement

will correspond to a large acceleration at higher frequencies, saturating the accelerometers. This was seen in experiments and the gain had to be reduced to prevent this.

As far as actuator choice the distributed strain actuator was superior in all cases. The distributed strain actuator was simpler to incorporate because it did not add a second degree of freedom. Furthermore, the distributed strain actuator is compact and performs better experimentally. This clearly shows that it is a better choice for future investigation.

An additional study was undertaken to study the spill-over effects (unintentionally exciting higher modes) and effects of accelerometer placement when patch actuators were used. The results showed that spill-over did occur, yet it was small, especially with the H_∞ controller. This was attributed to the noise rejection capacity of the H_∞ control method. The accelerometer placement also affected the results. The vibration suppression with the PVF controller was affected by the accelerometer placement while the H_∞ controller was less affected. This can be also attributed to the robust nature of this type of control.

Acknowledgements

The authors would like to thank Raytheon Aircraft Integration Systems for partial funding of this research.

References

[1] J.-H. Han, J. Tani, I. Lee, Multi-modal vibration control of smart composite plates, *Material Science Research Internations* 5 (2) (1999) 122–127.
[2] M. Serrand, S.J. Elliott, Multichannel feedback control for the isolation of base-excited vibration, *Journal of Sound and Vibration* 234 (2000) 681–704.
[3] L. Ray, B.-H. Koh, Integration of autonomous fatigue crack detection and vibration control in smart plates, *Proceedings of SPIE* 3985 (2000) 629–639.
[4] K.-H. Rew, J.-H. Han, I. Lee, Adaptive multi-modal vibration control of wing-like composite structure using adaptive positive position feedback, *41st AIAA/ASCE/AHS/ASC Structures, Structural Dynamics, and Materials Conference*, 2000 April, pp. 664–673.
[5] M. Valoor, K. Chandrashekhara, S. Agarwal, Active vibration control of smart composite plates using self adaptive neuro-controller, *Proceedings of SPIE* 3984 (2000) 256–267.
[6] P. Laura, D. Romanelli, Vibrations for rectangular plates elastically restrained against rotation along alledges and subject to a bi-axial state of stress, *Journal of Sound and Vibration* 37 (3) (1974) 367–377.
[7] E. Richer, *Using innovative control algorithms for better design of force actuators*, Southern Methodist University, Dallas, TX, 1999.
[8] L. Meirovitch, *Principles and Techniques of Vibrations*, Prentice-Hall, Upper Saddle River, NJ, 1997.
[9] E.K. Dimitriadis, C.R. Fuller, C.A. Rogers, Piezoelectric actuators for distributed vibration excitation of thin plates, *Journal of Vibration and Acoustics* 113 (1991) 100–107.
[10] R.T. Stefani, C.J. Savant Jr., B. Shahian, G.H. Hostetter, *Design of Feedback Control Systems*, Saunders College Publishing, Orlando, FL, 1994.
[11] A. Dimarogonas, *Vibrations for Engineers*, Prentice-Hall, Upper Saddle River, NJ, 1996.
[12] L. Lublin, S. Grocott, M. Athans, H2(LQG) and H_∞ control, in: *The Control Handbook*, IEEE Press, Rockville, MD, 1996, pp. 651–661.
[13] K. Zhou, J.C. Doyle, *Essentials of Robust Control*, Prentice-Hall, Upper Saddle River, NJ, 1998.